Modeling the Simultaneous Dropout of Energetic Electrons and Protons by Magnetopause Shadowing

Xingzhi Lyu [1], Weichao Tu [1], Jinbei Huang [1], Qianli Ma [2,3], and Zhi Gu Li[1]

1 Department of Physics and Astronomy, West Virginia University, Morgantown, West Virginia, USA

2 Department of Atmospheric and Oceanic Sciences, University of California, Los Angeles, CA, USA

3 Center for Space Physics, Boston University, Boston, MA, USA

Key points:

- A radial diffusion model with event-specific LCDS is used to simulate the concurrent dropout of electrons and protons due to magnetopause shadowing
- The model captures the fast shadowing loss of both populations at high L^* but not the loss at low L^* possibly from EMIC wave scattering
- The model reproduces the butterfly PAD of electrons in the initial loss phase but underestimates the loss of protons at low pitch angles

Abstract

Magnetopause shadowing (MPS) effect could drive a concurrent dropout of radiation belt electrons and ring current protons. However, its relative role in the dropout of both plasma populations has not been well quantified. In this work, we study the simultaneous dropout of MeV electrons and 100s keV protons during an intense geomagnetic storm in May 2017. A radial diffusion model with an event-specific last closed drift shell is used to simulate the MPS loss of both populations. The model well captures the fast shadowing loss of both populations at high L^*, while the loss at lower L^*, possibly due to the EMIC wave scattering, is not captured. The observed butterfly pitch angle distributions of electron fluxes in the initial loss phase are well reproduced by the model. The initial proton losses at low pitch angles are underestimated, potentially also contributed by other mechanisms such as field line curvature scattering.

Plain Language Summary

Magnetopause shadowing (MPS), due to the solar wind compression of the magnetopause combined with outward radial diffusion driven by Ultra Low Frequency (ULF) waves, is known to be one of the major loss mechanisms for both radiation belt electrons and ring current protons. However, the role of MPS in driving the simultaneous dropout of both populations has not been well quantified. In this study, for the first time, we quantitatively model the fast shadowing loss of radiation belt electrons and ring current protons during a geomagnetic storm event using a radial diffusion model with event-specific inputs. The results indicate that MPS can efficiently capture the concurrent fast depletion of both populations at high L^*.

1. Introduction

Several literatures have reported the simultaneous dropout of MeV radiation belt (RB) electrons and 100s keV ring current (RC) protons based on Van Allen Probes measurements (e.g., Turner et al., 2014; Zhao et al., 2016; Gkioulidou et al., 2016, Lyu et al., 2022b). The fundamental question is, where do these particles go during the dropout? Two main loss mechanisms have been identified by previous studies for radiation belt electron dropout (e.g., Morley et al., 2010; Shprits et al., 2016; Tu et al.,2014; Xiang et al., 2017, 2018), which includes the precipitation loss into the atmosphere due to the interaction with Electromagnetic Ion Cyclotron (EMIC) waves (e.g., Usanova et al., 2014; Blum et al., 2015; Ma et al., 2015; Zhang et al., 2016; Capannolo et al., 2019), and the loss through the outer boundary of the magnetosphere (i.e., the magnetopause), due to the solar wind compression combined with outward radial diffusion driven by Ultra-Low-Frequency (ULF) waves (e.g., Turner et al., 2012; Tu et al., 2019). Theoretically, both mechanisms can also lead to the loss of ring current protons, which are usually collocated with RB electrons.

The latter mechanism called magnetopause shadowing (MPS), which is the focus of this study, has been proved to be responsible for the fast losses of both radiation belt electrons and ring current protons (e.g., Liemohn et al., 1999; Tu et al., 2014), but its relative role in the simultaneous dropout of these two populations has not been well quantified compared to other loss processes. For radiation belt electrons, Tu et al. (2019) simulated the MPS loss of radiation belt electrons during June 2015 with realistic inputs. The model well captured the fast shadowing loss of electrons at high L^* regions after the arrival of two consecutive interplanetary shocks, and well reproduced the initial adiabatic loss of the high-energy storage ring at low L^* regions after

the second strong shock. For ring current protons, Kim et al. (2005) analyzed the average characteristics of solar wind dynamic pressure based on 95 geomagnetic storm events selected during the years of 1997-2002 and performed test particle orbit calculations using a simplified magnetopause model. They found that the solar wind dynamic pressure is enhanced during the storm main phase, which pushes the magnetopause to move inward. As a consequence, ring current particles can efficiently cross the magnetopause, leading to their subsequent loss. For comparative dropout studies of both populations, Turner et al. (2014) examined the evolution of flux versus L^* profiles for both MeV electrons and >100s keV protons during the 30 September 2012 storm and found concurrent dropout of energetic electrons and protons at $L^* > 4$ with similar features that are highly consistent with the MPS loss.

The previous studies discussed above have mainly focused on qualitative aspects or have only addressed one specific population, and hence, a comprehensive comparative study is needed to quantitatively study the role of magnetopause shadowing in the energetic particle distributions and variations. In this work, for the first time, we simulate the fast particle loss due to the magnetopause shadowing based on the measurements of Van Allen Probes during an intense geomagnetic storm in May 2017, to quantify the role of magnetopause shadowing in the simultaneous dropout of radiation belt electrons and ring current protons.

2. Event Analysis

The Van Allen Probes mission consists of two identical instrumented spacecrafts (A and B) operating in a near-equatorial ~9-hours orbit with an inclination of $\sim 10^{\circ}$, perigee of ~ 600 km and apogee of 5.8 R_E (Mauk et al., 2012). This orbit allows for the frequent sampling (e.g., completion of three obits during the main phase of a geomagnetic storm) inside the geosynchronous orbit, providing the high-resolution particle measurements used in this study. For energetic electrons, flux measurements made by Magnetic Electron Ion Spectrometer (MagEIS) (Blake et al., 2013) and Relativistic Electron Proton Telescope (REPT) instruments are utilized. The MagEIS instrument measures electrons over the energy range of ~ 30 keV to ~ 4 MeV, while REPT provides measurements for highly energetic electrons with energies ranging from ~ 1.5 MeV to ~ 20 MeV. For energetic protons, we make use of the flux measurements by Radiation Belt Storm Probes Ion Composition Experiment (RBSPICE) instrument (Mitchell et al., 2013) with an energy range of 10-600 keV.

Figure 1 presents an overview of the energetic electron (left column) and proton (right column) flux evolution during May 27-28, 2017, along Van Allen Probes' orbits. Figures 1a1-1a2 show the 1.08 and 4.2 MeV radiation belt electron fluxes at 90° local pitch angle as a function of time and dipole L shell, measured by the MagEIS and REPT instrument onboard Van Allen Probes. On the right-hand side, 121 and 328 keV ring current proton fluxes at 90° local pitch angle measured by RBSPICE instrument are plotted in the same way, as shown in Figures 1b1-1b2. The Sym-H index is shown in Figures 1a5 and 1b5, with a minimum value of ~ -150 nT indicating an intense geomagnetic storm. The observed fluxes for MeV electrons and 100s keV protons exhibited simultaneous dropout outside $L \sim 3.8$ during the storm main phase. These unidirectional differential fluxes for both populations during this event are then used to calculate the phase space density (PSD) (Chen et al., 2005; Lyu et al., 2022a) as a function of the three adiabatic invariants (μ, K, and L^*) in the Tsyganenko 04 storm time (TS04) magnetic field model (Tsyganenko & Sitnov, 2005) to remove the adiabatic variations and reveal the real particle loss during the dropout.

Figures 1a3-1a4 plot the electron PSD with μ=912 and 2290 MeV/G respectively and at K=0.11 $G^{1/2}R_E$ (corresponding to $\sim 2.2, 5.5$ MeV electrons at $L \sim 5$, respectively) versus time and L^*, while panels b3-b4 are plotted in the same way but for proton PSD with $\mu = 80$ and 100 MeV/G respectively and at $K = 0.11\ G^{1/2}R_E$ (corresponding to $\sim 190, 240$ keV protons at $L \sim 5$). Physical last closed drift shell (LCDS) values during this event are calculated using a test particle tracing method (Albert et al., 2018) based on the TS04 magnetic field model driven by real-time solar wind conditions. The LCDS at $K = 0.11\ G^{1/2}R_E$ is plotted as the black curves in Figures 1a3 and 1b3. We find that the LCDS was pushed to as low as $L^* = 4.6$ at ~ 00UT on 28 May in the beginning of the storm main phase and stay below $L^* = 5.2$ for the subsequent ~ 6 hours. Following the inward push of the LCDS to $L^* = 4.6$ and intersecting with Van Allen Probes' orbits, the calculated PSD for both radiation belt electrons and ring current protons shows a significant depletion in the regions above $L^* = 4.5$, and with stronger loss occurring at higher L^* across a wide range of μ. These concurrent dropout features for both populations at higher L^* region is consistent with the signatures of the loss induced by magnetopause shadowing and is the focus of this study.

3. Event Simulation

3.1. Radial Diffusion Model

To simulate the magnetopause shadowing loss and the associated outward radial diffusion of both radiation belt electrons and ring current protons during the May 2017 dropout event, we perform a radial diffusion model by solving the equation (Schulz & Lanzerotti, 1974):

$$\frac{\partial f}{\partial t} = L^2 \frac{\partial}{\partial L}\left(\frac{D_{LL}}{L^2}\frac{\partial f}{\partial L}\right) - \frac{f}{\tau},$$

where f is the electron/proton PSD at constant μ and K values, L is the Roederer L or L^*, D_{LL} is the radial diffusion coefficient, and τ is the e-folding lifetime of particles. To represent the loss effects of magnetopause shadowing, the electron/proton lifetimes outside the event-specific LCDS are set to be on the order of its drift periods (energy and pitch angle dependent). The model's outer boundary is defined at $L^* = 11$ (with Neumann boundary condition $\partial f/\partial L = 0$) which is always outside the LCDS during this dropout event (Tu et al., 2019). The initial conditions as a function of L^* for both populations are derived from the first available PSD data during the event. For the diffusion coefficient, the empirical D_{LL} as a function of Kp and L (approximately regarded as L^*) are used in the model with the magnetic component from Brautigam and Albert (2000) and the electric component from Brautigam et al. (2005).

3.2. Simulation Results in PSD

With the model setups described above, Figure 2a2 shows the simulation results for radiation belt electrons with the same μ and K values in Figure 2a1 which shows the electron PSD observations. The black curve in Figure 2a1 and the white curve in Figure 2a2 denotes the LCDS position. The simulation results show that fast shadowing loss of RB electrons are captured by the model. To perform a more detailed comparison between model and data, three different time intervals are selected to calculate the averaged PSD versus L^* profiles within each interval. The time coverage of each interval is marked by the horizontal color bars between Figures 2a1 and 2a2 and denoted in UT hours in Figure 2c1. Figures 2c1 and 2c2 show the evolution of PSD versus L^* profiles during these intervals from the data and model, respectively. The black curves are profiles during interval #1 which covers the pre-storm interval. The data and model exhibit similar profiles with mostly positive gradient of PSD versus L^*. Then for interval #2 during the initial phase of the storm, which encloses a small LCDS drop, the observed PSD data drops

outside $L^* = 4.5$ shown as the blue profiles in Figure 2c1, while the model results in Figure 2c2 only capture slight losses. During interval #3, which corresponds to the storm main phase, the LCDS was pushed to as low as $L^* \sim 4.6$ and remained below $L^* = 5.2$ throughout this period. The modeled PSD in panel (c2) presents stronger losses at higher L^* ($L^* > 4.6$) that are consistent with the loss features driven by the magnetopause shadowing effect. Comparing with the observations, the model in interval #3 generally captures the shadowing loss at higher L^* (close to $L^* = 5.5$) even though it is slightly underestimated at $L^* < 4.8$. The under-produced loss at high L^* regions in the model for both intervals #2 and #3 makes us wonder if the empirical model of D_{LL} is realistic during this dropout event. As a simple test, we increase D_{LL} by a factor of 5 and the new simulation results are shown in panel (c3). By comparing between model results in panels (c2) and (c3) against the observations in panel (c1), we find a stronger radial diffusion coefficient indeed helps to better capture the shadowing loss at high L^* ($L^* > 4.6$) during both the storm initial and main phases. In addition, we note that for the region at $L^* < 4.6$, there are two local dips in the observed PSD profile (Figure 2c1) at $L^* \sim 3.7$ and 4.4, respectively. These local dips could possibly be induced by some localized scattering effect due to the interactions with plasma waves (e.g., EMIC waves), that are not included by the current 1D radial diffusion model and is not the focus of this work.

For ring current protons, Figure 2b2 plots the simulation results with the same μ and K values as the proton PSD data in Figure 2b1. Same as electrons, three time intervals are selected to investigate the detailed PSD evolution along L^*. The profiles for each time interval are plotted in panels (d1) (PSD data) and panel (d2) (model with original empirical D_{LL}). The findings are very similar to electrons. During interval #1, the black curves in both data and model show generally consistent positive PSD versus L^* gradients. Then for interval #2, the PSD data represented by the blue profile drops slightly at $L^* > 5.3$ and forms a local peak at $L^* = 5.2$. Similar to electrons, the model results in panel (d2) barely show any losses at higher L^*. Finally, during interval #3, the red data profile in panel (d1) presents significant shadowing losses outside $L^* = 4.6$, which are generally captured by the model as depicted in panel (d2) but slightly under-reproduced. Similarly, we try to simply increase the empirical D_{LL} by a factor of 5 and find that the new simulation results shown in panel (d3) again better capture the observed losses at high L^* for both intervals #2 and #3. The simple test we performed on adjusting D_{LL} suggests that it is

likely that the empirical D_{LL} model we used in the simulation may underestimate the radial diffusion rate during this dropout event. Implementing more realistic and event-specific D_{LL} is part of our future work but out of the scope of this study. Additionally, likewise to electrons, there exists a similar local dip in the observed proton PSD profile during the storm main phase (red profile in panel (d1)) at $L^* \sim 4.4$, which may also result from the scattering effects by EMIC waves that are not included in the model.

3.3 Simulation in Flux

The comparison between PSD data and model results analyzed above is for a fixed μ and K values. To obtain a better understanding of the loss mechanisms, the simulations are performed covering a wider range of μ and K values. Then the modeled PSD is converted to flux by using the TS04 model to directly compare with the flux observations. Note that for the flux simulations, original D_{LL} values from the empirical models are used.

Panels (a1) and (a2) in Figure 3 compare the observed and modeled electron fluxes at 2.1 MeV and $90°$ local pitch angle. Panel (a1) shows the observed flux versus time and L^*, while panel (a2) shows the modeled flux along Van Allen Probes' orbit. The comparison indicates that our model well captures the shadowing loss at higher L^* during the storm's initial phase (interval #2), as well as the more significant losses during main phase (interval #3). As the magnetopause is pushed inward during geomagnetic active periods, the LCDS reaches lower L^* values for higher pitch angles due to the drift shell splitting effects (e.g., Tu et al., 2019). This can lead to the formation of butterfly-shaped pitch angle distribution of fluxes at higher L shells. In panels (a3) and (a4) we compare the observed and modeled pitch angle distributions of electron fluxes at 2.1 MeV along Van Allen Probe A's orbit. The butterfly pitch angle distribution is observed during the initial loss and is shown to be well captured by the model, especially between $60° - 120°$. Outside that pitch angle range (i.e., at lower pitch angles), the model slightly underestimates the observed losses. This could potentially be due to the uncertainty from the radial diffusion coefficient, since its dependence on the pitch angle is still not well understood or quantified (e.g., Sarris et al., 2022). Moreover, by checking the wave measurements during this time, we find that EMIC waves are present (not shown), which could also possibly contribute to the observed losses at lower pitch angles. For the later storm main phase (after interval #3), the observed pitch angle distribution in panel (a3) shows fast dropout over all the pitch angles (the black region)

when Van Allen Probe A is located at a high L^* region, which is well reproduced by the model in panel (a4).

On the right-hand side, panels (b1) and (b2) compare the observed and modeled proton fluxes at 220 keV and 90° local pitch angle along the two probes' orbits. The comparison indicates that the model slightly overestimates the observed shadowing loss of protons at 90° local pitch angle during the initial loss phase (interval #2). Later in interval #3 during the storm main phase, the model results generally capture the high L^* loss compared to data with slight overestimation as well. Panels (b3) and (b4) compare the observed and modeled pitch angle distributions of 220 keV protons along Van Allen Probe A's orbit. Different from electrons, during interval #2, observed proton fluxes in panel (b3) show nearly isotropic pitch angle distributions at higher L shells (L~5.7) rather than clear butterfly distributions as in electrons. However, the simulation results in panel (b4) still show a butterfly pitch angle distribution, slightly overestimating the losses close to 90° local pitch angle and underestimating the loss at lower pitch angles ($< 40°$). Similar to electrons, these discrepancies could be due to the uncertainty of the radial diffusion coefficient and its pitch angle dependence. For the potential contribution from EMIC waves, we calculate the diffusion rates based on quasi-linear theory driven by in-situ EMIC wave measurements. The results suggest that it may take several hours for the observed EMIC waves to scatter 100s keV protons at lower pitch angles, which may also contribute to the observed fast proton losses (Lyu et al., 2022b). On the other hand, previous studies have demonstrated that the ring current ions can also be influenced by field line curvature (FLC) scattering (e.g., Delcourt et al., 1996; Eshetu et al., 2020; Yu et al., 2020). FLC scattering occurs when the radius of the field line curvature is comparable to the particle's gyro-radius. To investigate such a scenario, we calculate the adiabaticity parameter ϵ (defined as the ratio between the particles gyro-radius and the radius of the field line curvature) based on TS04 magnetic field model, which serves a criterion for FLC scattering effects. When probe A observed the isotropic pitch angle distribution of the 220 keV proton population in panel (b3), near $L \sim 5.7$ and MLT=18.1 at 23 UT of May 27, the calculated ϵ is found to be 0.15, above the critical threshold ($\epsilon = 0.1$) for strong FLC scattering effect to occur (e.g., Dubyagin et al., 2018; Yu et al., 2020). This suggests that the FLC scattering effects may have significant contributions to the formation of isotropic pitch angle distribution and the observed proton loss at lower pitch angles. For further validation, we investigate the low-altitude measurements to look for the isotropic boundary (IB) often

associated with the FLC scattering processes (e.g., Dubyagin et al., 2018; Ganushkina et al., 2005; Sergeev et al., 1993). NOAA-19 observations confirm the presence of an IB at $L \sim 5$ for 100s keV protons at similar UT and MLT (not shown). This signifies that 100s keV protons at L values above the IB could undergo significant FLC scattering effects, which subsequently results in additional scattering and losses. Finally, for the later storm main phase after interval #3, Van Allen Probe A also observed fast loss of protons over a wide range of pitch angles in panel (3), which are also captured by the model results in panel (b4), though slightly over-reproduced.

4. Conclusions and Discussions

Simultaneous dropout between MeV radiation belt electrons and 100s keV ring current protons at high and low L regions were observed by the Van Allen Probes during an intense storm in May 2017. Here, for the first time, a radial diffusion model with an event-specific LCDS calculated by a physical test particle tracing code is implemented to quantitatively simulate the concurrent losses of both particle populations due to magnetopause shadowing effect during the dropout event. The major findings are concluded as follows:

1. The concurrent dropouts between MeV radiation belt electrons and 100s keV ring current protons at high L^* regions both show the features including stronger loss at higher L^*, and loss across a wide range of μ values (energies). These signatures indicate that the observed fast losses could be dominated by magnetopause shadowing effect.
2. Our radial diffusion model with event-specific LCDS generally captures the observed high L^* losses for both populations during the storm main phase, while the losses at low L^* regions ($L^* \sim 4.4$ for both populations and $L^* \sim 3.7$ for electrons only) are not captured, which are possibly due to the scattering effect by the interactions with EMIC waves. Increasing the rate of radial diffusion could further improve the model performance at high L^* regions during both the storm initial and main phases.
3. For MeV radiation belt electrons, butterfly pitch angle distributions of their fluxes are observed at higher L shells (e.g., $L \sim 5.7$) in the initial loss phase, which are well reproduced by the model. Specifically, strong consistency is obtained between observed and modeled fluxes at pitch angles ranging from $60° - 120°$. However, losses outside this range are underestimated by the model, possibly due to the uncertainty from the radial diffusion coefficient and/or the local interactions with EMIC waves.

4. In contrast to the electrons, the observed 100s keV ring current proton fluxes show isotropic pitch angle distributions at high L shells in the initial loss phase. Similar to electrons, the modeled proton fluxes exhibit butterfly pitch angle distributions, which underestimate the losses at $< 40°$ (or $> 140°$) pitch angles. This discrepancy could be due to the uncertainty from the radial diffusion coefficient, or the potential contributions from EMIC wave scattering and FLC scattering effect on energetic protons.

In summary, the observed concurrent dropouts at high L^* for both radiation belt electrons and ring current protons during the storm event are well explained by magnetopause shadowing effects and quantitatively reproduced by our 1D radial diffusion model with realistic LCDS input. To include other loss mechanisms such as localized EMIC wave scattering and FLC scattering, a more comprehensive model (e.g., RAM-SCB model) is needed and will be utilized in the future to further investigate the energetic particle dropout in the Earth's outer radiation belt and ring current.

Acknowledgements

This work was supported by NASA grants 80NSSC19K0908, 80NSSC21K1312, and 80NSSC21K2008, DOE grant DE-SC0020294, and NSF Grant AGS 1752736. QM would like to acknowledge the NASA grant 80NSSC20K0196 and NSF grant AGS-2225445. We acknowledge the Van Allen Probes data from MagEIS and REPT instrument, as well as the MagEphem data obtained from https://rbsp-ect.newmexicoconsortium.org/science/DataDirectories.php, data from RBSPICE instrument obtained from http://rbspice.ftecs.com/Data.html.

Open Research

The model inputs and outputs in this paper are publicly available from the data repository https://doi.org/10.5281/zenodo.8400527.

References

Albert, J. M., Selesnick, R. S., Morley, S. K., Henderson, M. G., & Kellerman, A. C. (2018). Calculation of last closed drift shells for the 2013 GEM radiation belt challenge events. Journal

of Geophysical Research: Space Physics, 123(11), 9597–9611. https://doi.org/10.1029/2018JA025991

Blake, J.B., Carranza, P.A., Claudepierre, S.G. et al. The Magnetic Electron Ion Spectrometer (MagEIS) Instruments Aboard the Radiation Belt Storm Probes (RBSP) Spacecraft. Space Sci Rev 179, 383–421 (2013). https://doi.org/10.1007/s11214-013-9991-8

Blum, L. W., Halford, A., Millan, R., Bonnell, J. W., Goldstein, J., Usanova, M., Engebretson, M., Ohnsted, M., Reeves, G., Singer, H., et al. (2015), Observations of coincident EMIC wave activity and duskside energetic electron precipitation on 18–19 January 2013, Geophys. Res. Lett., 42, 5727– 5735, doi:10.1002/2015GL065245.

Brautigam, D. H., & Albert, J. M. (2000). Radial diffusion analysis of outer radiation belt electrons during the 9 October 1990 magnetic storm. Journal of Geophysical Research, 105(A1), 291–309. https://doi.org/10.1029/1999JA900344

Brautigam, D. H., Ginet, G. P., Albert, J. M., Wygant, J. R., Rowland, D. E., Ling, A., & Bass, J. (2005). CRRES electric field power spectra and radial diffusion coefficients. Journal of Geophysical Research, 110, A02214. https://doi.org/10.1029/2004JA010612

Capannolo, L., Li, W., Ma, Q., Shen, X.-C., Zhang, X.-J., Redmon, R. J., et al. (2019). Energetic electron precipitation: Multievent analysis of its spatial extent during EMIC wave activity. Journal of Geophysical Research: Space Physics, 124, 2466– 2483. https://doi.org/10.1029/2018JA026291

Chen, Y., Friedel, R. H. W., Reeves, G. D., Onsager, T. G., and Thomsen, M. F. (2005), Multisatellite determination of the relativistic electron phase space density at geosynchronous orbit: Methodology and results during geomagnetically quiet times, J. Geophys. Res., 110, A10210, doi:10.1029/2004JA010895.

Delcourt, D. C., Sauvaud, J.-A., Martin, R. F., and Moore, T. E. (1996), On the nonadiabatic precipitation of ions from the near-Earth plasma sheet, J. Geophys. Res., 101(A8), 17409–17418, doi:10.1029/96JA01006.

Dubyagin, S., Ganushkina, N. Y., & Sergeev, V. A. (2018). Formation of 30 keV proton isotropic boundaries during geomagnetic storms. Journal of Geophysical Research: Space Physics, 123, 3436–3459. https://doi.org/10.1002/2017JA024587.

Eshetu, W. W., Tu, W., Jordanova, V. K., & Cowee, M. (2021). Quantifying the effect of magnetic field line curvature scattering on the loss of ring current ions. Journal of Geophysical Research: Space Physics, 126, e2020JA028497. https://doi.org/10.1029/2020JA028497.

Ganushkina, N. Yu., Pulkkinen, T. I., Kubyshkina, M. V., Sergeev, V. A., Lvova, E. A., Yahnina, T. A., Yahnin, A. G., and Fritz, T.: Proton isotropy boundaries as measured on mid- and low-altitude satellites, Ann. Geophys., 23, 1839–1847, https://doi.org/10.5194/angeo-23-1839-2005, 2005.

Gkioulidou, M., Ukhorskiy, A. Y., Mitchell, D. G., and Lanzerotti, L. J. (2016), Storm time dynamics of ring current protons: Implications for the long-term energy budget in the inner magnetosphere, Geophys. Res. Lett., 43, 4736– 4744, doi:10.1002/2016GL068013.

Kim, K. C., Lee, D.-Y., Lee, E. S., Choi, C. R., Kim, K. H., Moon, Y. J., Cho, K. S., Park, Y. D., and Han, W. Y. (2005), A new perspective on the role of the solar wind dynamic pressure in the ring current particle loss through the magnetopause, J. Geophys. Res., 110, A09223, doi:10.1029/2005JA011097.

Liemohn, M. W., Kozyra, J. U., Jordanova, V. K., Khazanov, G. V., Thomsen, M. F., & Cayton, T. E. (1999). Analysis of early phase ring current recovery mechanisms during geomagnetic storms. Geophysical Research Letters, 26(18), 2845–2848. https://doi.org/10.1029/1999GL900611

Lyu, X., & Tu, W. (2022a). Modeling the dynamics of energetic protons in Earth's inner magnetosphere. Journal of Geophysical Research: Space Physics, 127, e2021JA030153. https://doi.org/10.1029/2021JA030153

Lyu, X., Ma, Q., Tu, W., Li, W., & Capannolo, L. (2022b). Modeling the simultaneous dropout of energetic electrons and protons by EMIC wave scattering. Geophysical Research Letters, 49, e2022GL101041. https://doi.org/10.1029/2022GL101041

Ma, Q., Li, W., Thorne, R. M., Ni, B., Kletzing, C. A., Kurth, W. S., Hospodarsky, G. B., Reeves, G. D., Henderson, M. G., Spence, H. E., Baker, D. N., Blake, J. B., Fennell, J. F., Claudepierre, S. G. and Angelopoulos, V. (2015), Modeling inward diffusion and slow decay of energetic electrons in the Earth's outer radiation belt. Geophys. Res. Lett., 42: 987– 995. doi: 10.1002/2014GL062977.

Mauk, B.H., Fox, N.J., Kanekal, S.G. et al. Science Objectives and Rationale for the Radiation Belt Storm Probes Mission. Space Sci Rev 179, 3–27 (2013). https://doi.org/10.1007/s11214-012-9908-y

Mitchell, D.G., Lanzerotti, L.J., Kim, C.K. et al. Radiation Belt Storm Probes Ion Composition Experiment (RBSPICE). Space Sci Rev 179, 263–308 (2013). https://doi.org/10.1007/s11214-013-9965-x

Sarris, T. E., Li, X., Zhao, H., Papadakis, K., Liu, W., Tu, W., et al. (2022). Distribution of ULF wave power in magnetic latitude and local time using THEMIS and Arase measurements. *Journal of Geophysical Research: Space Physics*, *127*, e2022JA030469. https://doi.org/10.1029/2022JA030469

Schulz, M., & Lanzerotti, L. (1974). Particle diffusion in the radiation belts. Springer.

Sergeev, V. A., Malkov, M., and Mursula, K. (1993), Testing the isotropic boundary algorithm method to evaluate the magnetic field configuration in the tail, J. Geophys. Res., 98(A5), 7609–7620, doi:10.1029/92JA02587.

Tsyganenko, N. A., & Sitnov, M. I. (2005). Modeling the dynamics of the inner magnetosphere during strong geomagnetic storms. Journal of Geophysical Research, 110, A03208. https://doi.org/10.1029/2004JA010798

Tu, W., Cunningham, G. S., Chen, Y., Morley, S. K., Reeves, G. D., Blake, J. B., … Spence, H. (2014). Event-specific chorus wave and electron seed population models in DREAM3D using the Van Allen Probes. Geophysical Research Letters, 41, 1359–1366. https://doi.org/10.1002/2013GL058819

Tu, W., Xiang, Z., & Morley, S. K. (2019). Modeling the magnetopause shadowing loss during the June 2015 dropout event. Geophysical Research Letters, 46, 9388–9396. https://doi.org/10.1029/2019GL084419

Turner, D. L., Shprits, Y., Hartinger, M., & Angelopoulos, V. (2012). Explaining sudden losses of outer radiation belt electrons during geomagnetic storms. Nature Physics, 8(3), 208–212. https://doi.org/10.1038/nphys2185

Turner, D. L., et al. (2014), On the cause and extent of outer radiation belt losses during the 30 September 2012 dropout event, J. Geophys. Res. Space Physics, 119, 1530–1540, doi:10.1002/2013JA019446.

Usanova, M. E., et al. (2014), Effect of EMIC waves on relativistic and ultrarelativistic electron populations: Ground-based and Van Allen Probes observations, Geophys. Res. Lett., 41, 1375–1381, doi:10.1002/2013GL059024.

Xiang, Z., Tu, W., Li, X., Ni, B., Morley, S. K., & Baker, D. N. (2017). Understanding the mechanisms of radiation belt dropouts observed by Van Allen Probes. Journal of Geophysical Research: Space Physics, 122, 9858–9879. https://doi.org/10.1002/2017JA024487

Xiang, Z., Tu, W., Ni, B., Henderson, M. G., & Cao, X. (2018). A statistical survey of radiation belt dropouts observed by Van Allen Probes. Geophysical Research Letters, 45, 8035–8043. https://doi.org/10.1029/2018GL078907

Yu, Y., Tian, X., & Jordanova, V. K. (2020). The effects of field line curvature (FLC) scattering on ring current dynamics and isotropic boundary. Journal of Geophysical Research: Space Physics, 125, e2020JA027830. https://doi.org/10.1029/2020JA027830.

Zhang, X.-J., et al. (2016), Direct evidence for EMIC wave scattering of relativistic electrons in space, J. Geophys. Res. Space Physics, 121, 6620– 6631, doi:10.1002/2016JA022521.

Zhao, H., Li, X., Baker, D. N., Claudepierre, S. G., Fennell, J. F., Blake, J. B., Larsen, B. A., Skoug, R. M., Funsten, H. O., Friedel, R. H. W., et al. (2016), Ring current electron dynamics during geomagnetic storms based on the Van Allen Probes measurements, J. Geophys. Res. Space Physics, 121, 3333– 3346, doi:10.1002/2016JA022358.

Figures and Captions

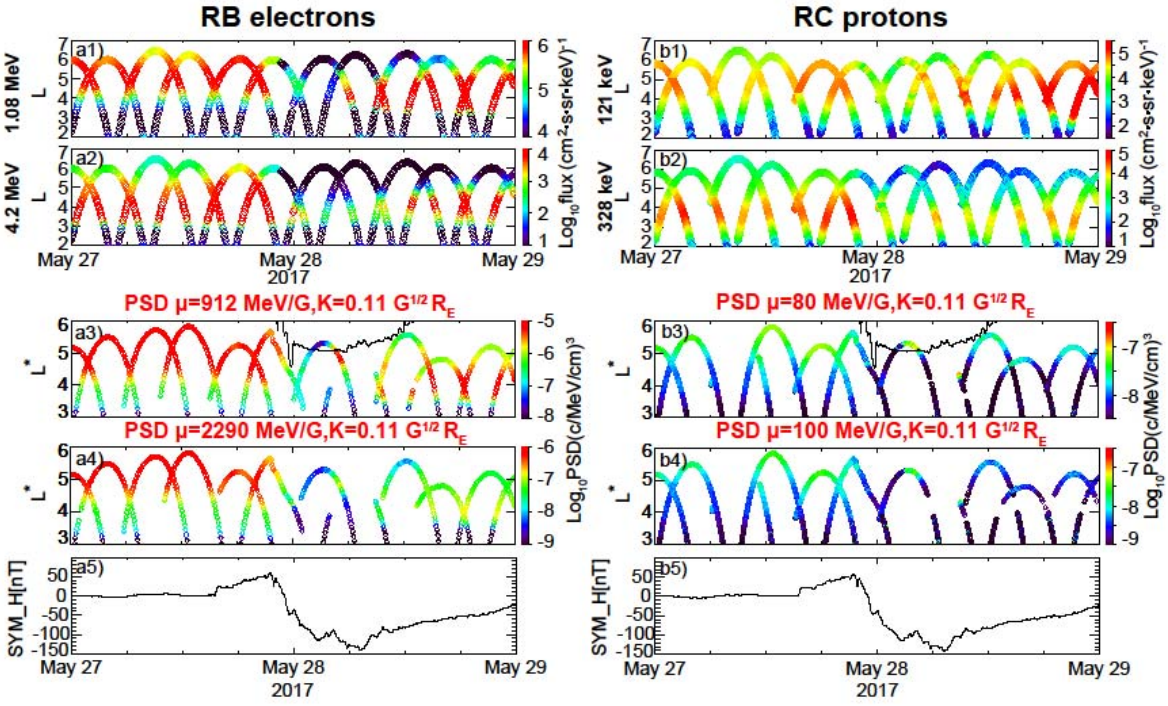

Figure 1. Panel a1- a2: Flux of (a1) 1.08 MeV and (a2) 4.2 MeV electrons with 90° local pitch angle versus time and L measured by MagEIS and REPT instruments onboard Van Allen Probes during May 27-28, 2017. Panels b1– b2: Flux of (b1) 121 keV, (b2) 328 keV protons with 90° local pitch angle versus L and time measured by RBSPICE instrument during the same time period as of electrons. Panels a3-a4, b3-b4: Phase Space Density (PSD) of (a3) $\mu = 912\,MeV/G$, (a4) $\mu = 2290\,MeV/G$ and $K = 0.11\,G^{1/2}R_E$ electrons, (b3) $\mu = 80\,MeV/G$, (b4) $\mu = 100\,MeV/G$ and $K = 0.11\,G^{1/2}R_E$ protons as a function of time and L^*. Black curves in panels (a3), (b3) represent the location of Last Closed Drift Shell (LCDS) at $K = 0.11\,G^{1/2}R_E$. Panels (a5, b5): SYM-H index.

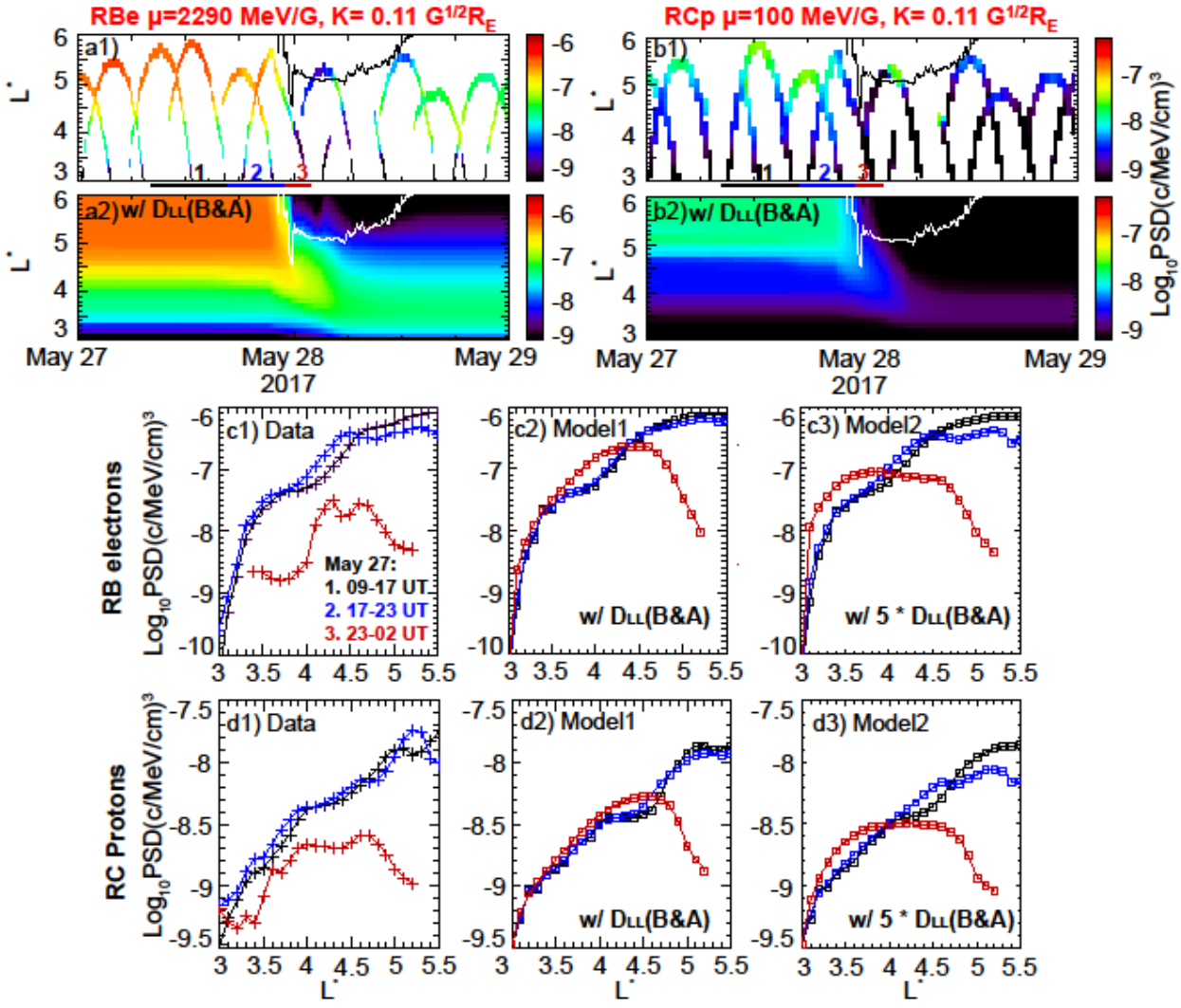

411
412

413 **Figure 2.** (a1-a2) Electron PSD data and simulation results at $\mu = 2290\,MeV/G$ and $K =$
414 $0.11\,G^{1/2}R_E$, and (b1-b2) proton PSD data and simulation results at $\mu = 100\,MeV/G$ and
415 $K = 0.11\,G^{1/2}R_E$, with the black line in panels (a1-b1) and white line in panels (a2-b2)
416 representing the location of Last Closed Drift Shell (LCDS). Observed and simulated (c1-c3)
417 electron and (d1-d3) proton PSD versus L^* profiles averaged over three different time intervals.

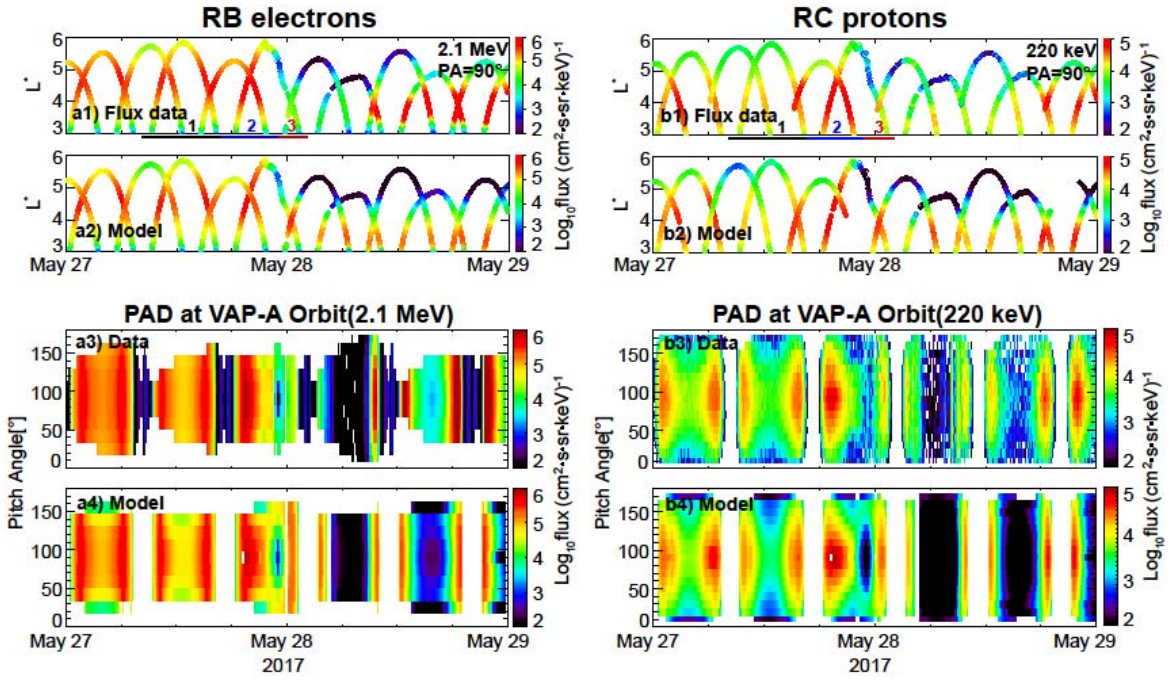

418

419 **Figure 3.** Observed and modeled (a1-a2) 2.1 MeV electron and (b1-b2) 220 keV proton fluxes at
420 90° local pitch angle along Van Allen Probes' orbits during 27-28 May 2017. Observed and
421 modeled pitch angle distributions of (a3-a4) 2.1 MeV electron (b3-b4) 220 keV proton fluxes
422 along Van Allen Probe A's orbit.

Figure 1.

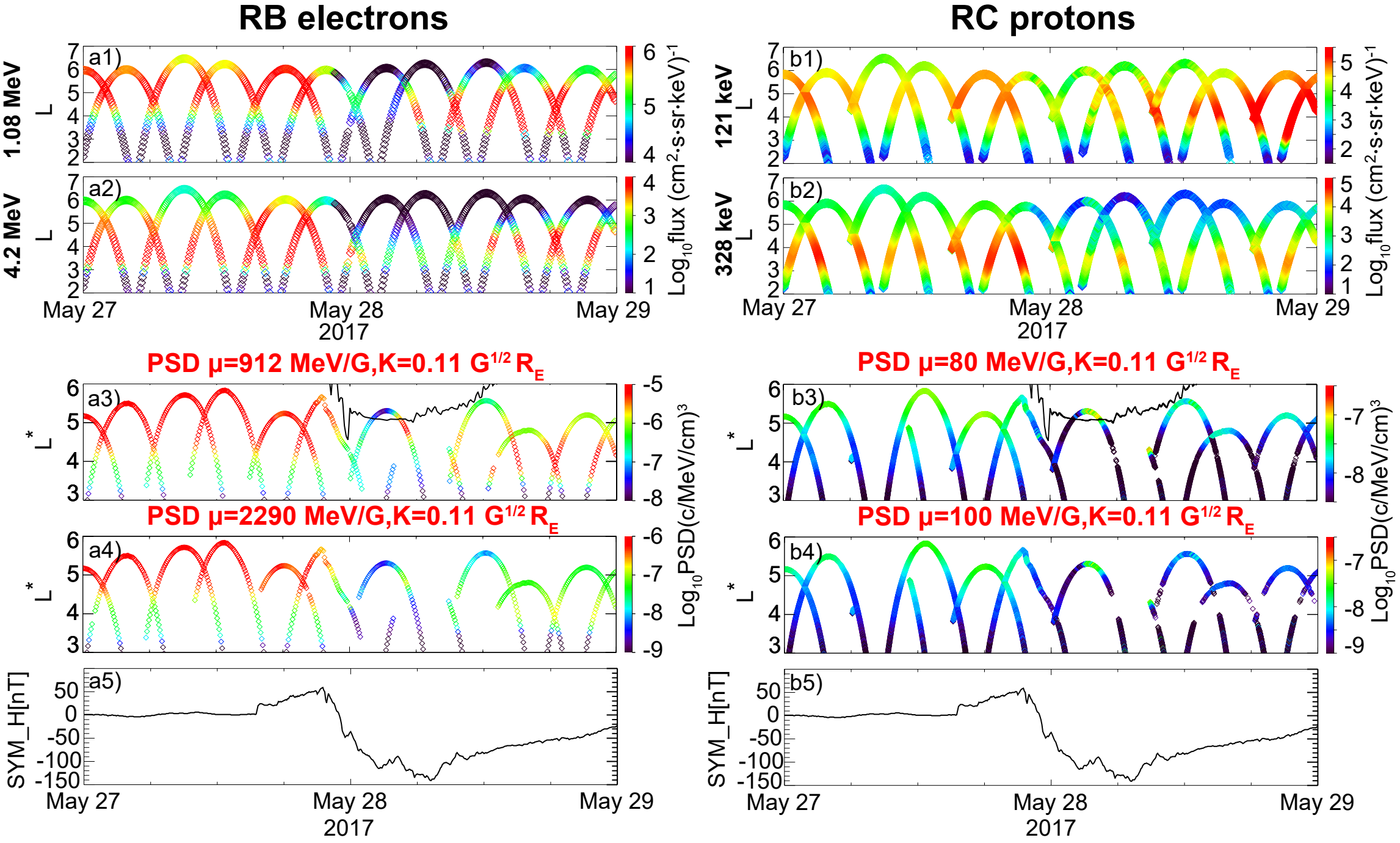
RB electrons
RC protons
1.08 MeV
4.2 MeV
121 keV
328 keV
a1)
a2)
b1)
b2)
L
Log10flux (cm2·s·sr·keV)-1
May 27
May 28
May 29
2017
PSD μ=912 MeV/G,K=0.11 G1/2 RE
PSD μ=2290 MeV/G,K=0.11 G1/2 RE
PSD μ=80 MeV/G,K=0.11 G1/2 RE
PSD μ=100 MeV/G,K=0.11 G1/2 RE
a3)
a4)
b3)
b4)
L*
Log10PSD(c/MeV/cm)3
a5)
b5)
SYM_H[nT]

Figure 2.

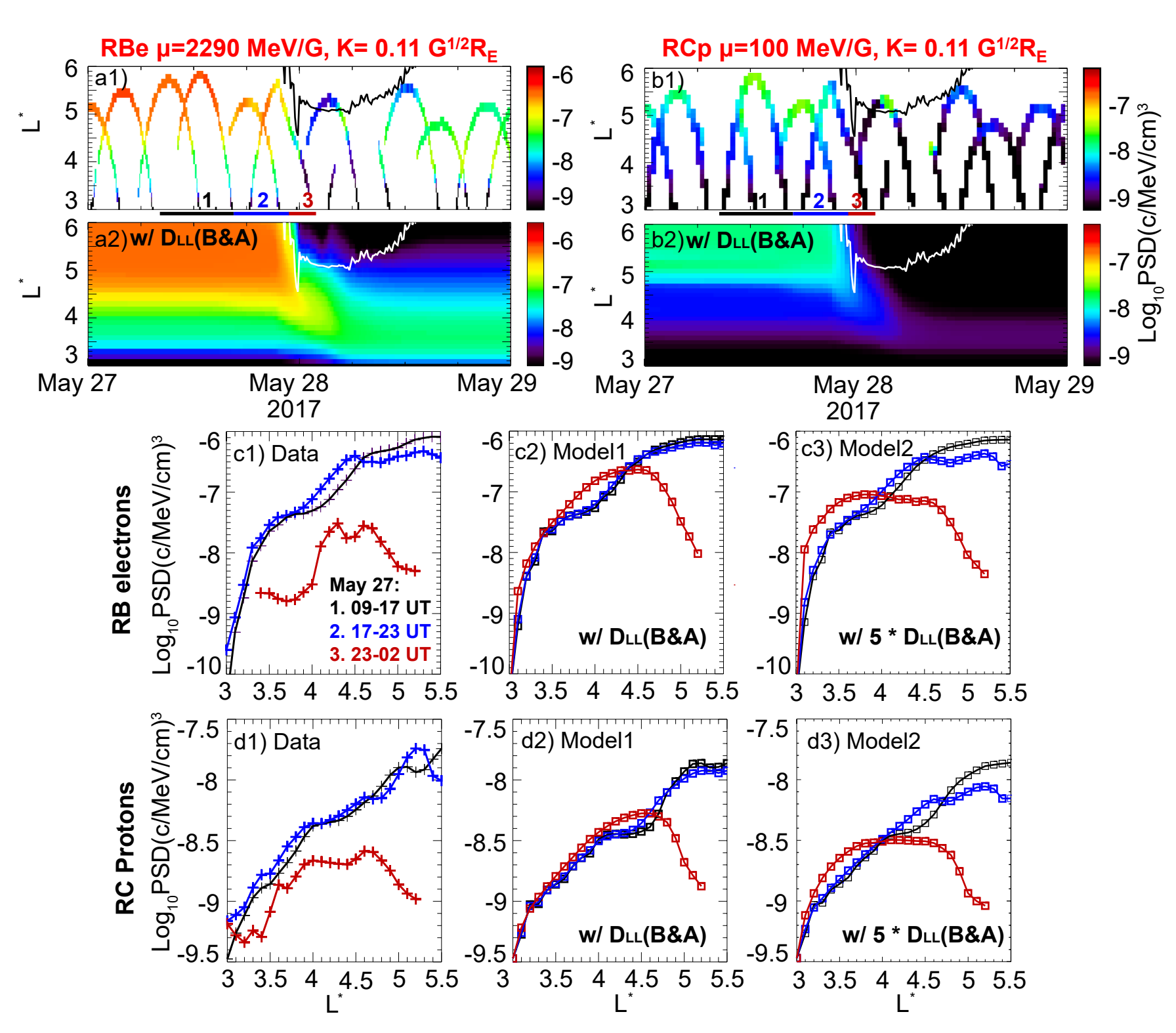
RBe μ=2290 MeV/G, K= 0.11 G^1/2R_E
RCp μ=100 MeV/G, K= 0.11 G^1/2R_E
a1)
b1)
a2)w/ DLL(B&A)
b2)w/ DLL(B&A)
L*
Log10PSD(c/MeV/cm)3
1
2
3
May 27
May 28
2017
May 29
RB electrons
RC Protons
c1) Data
c2) Model1
c3) Model2
d1) Data
d2) Model1
d3) Model2
May 27:
1. 09-17 UT
2. 17-23 UT
3. 23-02 UT
w/ DLL(B&A)
w/ 5 * DLL(B&A)

Figure 3.

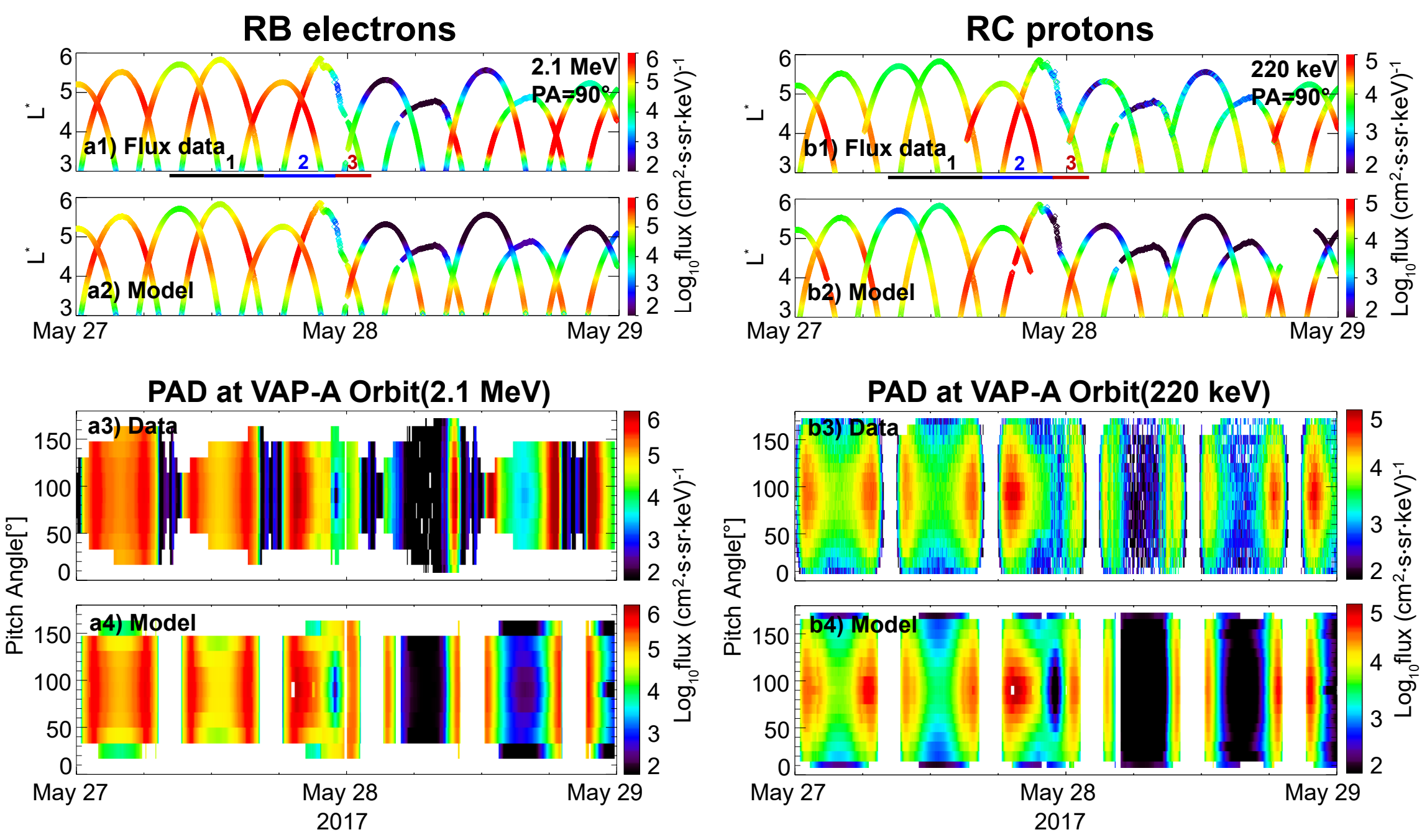
RB electrons
RC protons
2.1 MeV
PA=90°
220 keV
PA=90°
a1) Flux data
b1) Flux data
a2) Model
b2) Model
1
2
3
L*
Log10flux (cm2·s·sr·keV)-1
PAD at VAP-A Orbit(2.1 MeV)
PAD at VAP-A Orbit(220 keV)
a3) Data
b3) Data
a4) Model
b4) Model
Pitch Angle[°]
May 27
May 28
May 29
2017